Journal of Hazardous Materials 399 (2020) 123085

Contents lists available at ScienceDirect

Journal of Hazardous Materials

journal homepage: www.elsevier.com/locate/jhazmat

S-TiO_2/UiO-66-NH_2 composite for boosted photocatalytic Cr(VI) reduction and bisphenol A degradation under LED visible light

Yu-Xuan Li[a], Xun Wang[a], Chong-Chen Wang[a,*], Huifen Fu[a], Yanbiao Liu[b], Peng Wang[a], Chen Zhao[a]

[a] Beijing Key Laboratory of Functional Materials for Building Structure and Environment Remediation, School of Environment and Energy Engineering, Beijing University of Civil Engineering and Architecture, Beijing 100044, China

[b] Textile Pollution Controlling Engineering Center of Ministry of Environmental Protection, College of Environmental Science and Engineering, Donghua University, 2999 North Renmin Road, Shanghai 201620, China

GRAPHICAL ABSTRACT

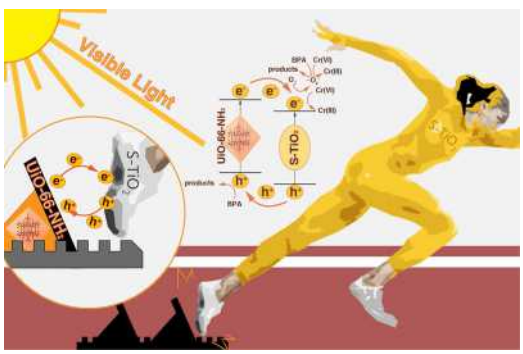

ARTICLE INFO

Editor: Navid B Saleh

Keywords:
UiO-66-NH_2
Sulfur-doped TiO_2
Hexavalent chromium
Bisphenol A
Photocatalysis

ABSTRACT

Series sulfur-doped TiO_2/amine-functionalized zirconium metal organic frameworks (S-TiO_2/UiO-66-NH_2) composites (U1T*x*) were facilely fabricated from the as-prepared S-TiO_2 and UiO-66-NH_2 via ball-milling method. The photocatalytic activities of U1T*x* toward Cr(VI) reduction and bisphenol A (BPA) degradation were tested under low-power LED visible light. The results demonstrated that U1T3 exhibited better photocatalytic performances than the pristine S-TiO_2 and UiO-66-NH_2 due to the improved separation and migration of electrons and holes. Furthermore, the influence factors like pH values and foreign ions on the photocatalytic performances of U1T*x* were also investigated. The Box-Behnken design methodology was utilized to further clarify that the inorganic foreign anions and dissolved organic matters could exert significant effects on photocatalytic Cr(VI) reduction performance. As well, the possible pathway of BPA degradation was depicted. After four runs of Cr(VI) removal, it was found that U1T3 exhibited preferable reusability and water stability. The probable reaction mechanism was proposed and verified by active species capture experiments, electron spin resonance determination and electrochemical analyses.

* Corresponding author.
E-mail addresses: wangchongchen@bucea.edu.cn, chongchenwang@126.com (C.-C. Wang).

https://doi.org/10.1016/j.jhazmat.2020.123085
Received 25 February 2020; Received in revised form 19 May 2020; Accepted 29 May 2020
Available online 04 June 2020
0304-3894/

1. Introduction

Various pollutants like heavy metals as well as organic pollutants are typically found in wastewater, which were toxic and could not be treated directly via biological process (Wang et al., 2016a, 2014). Among them, the widespread hexavalent chromium (Cr(VI)) and 4′-isopropylidenediphenol (bisphenol A, BPA) were harmful to both humans environment, leading to increasing concerns (Xu et al., 2009; Ellis, 2006). Cr(VI) often emerges in industries like electroplating, textile, and leather, which is presented with a wide range from 0.5–270.0 mg L^{-1} in surface water and wastewater (Testa et al., 2004; Li et al., 2019a). The existence of Cr(VI) in the environment poses a potential risk for liver, kidney and skin cancers in humans (Hu et al., 2005). The continuous introduction of organic pollutants like PPCPs into the environment could lead to adverse effects on aquatic and terrestrial organisms (Barceló and Petrovic, 2007). Bisphenol A (BPA), as a typical PPCPs, is universally found in packaging materials, electrical equipment, and eyeglass lenses (Canale et al., 2010). BPA is chemically stable and recalcitrant, which could be widely detected in urban wastewaters and treated effluents (Wang et al., 2016b; Subagio et al., 2010). Therefore, it is essential to develop new technologies for removing multiple pollutants from water.

Up to now, photocatalysis has been widely investigated for water purification. The photocatalytic reduction of Cr(VI) to Cr(III) is regarded as one of the most effective methods to remove Cr(VI), due to that Cr(III) is less toxic and can be easily removed by forming $Cr(OH)_3$ precipitate (Du et al., 2019a; Zhou et al., 2019). Some strategies like adsorption, biological treatment and thermal decomposition were adopted to remove BPA. However, these methods usually suffered from the disadvantages of incomplete destruction, time consuming and energy input (Subagio et al., 2010). In all, photocatalytic Cr(VI) reduction and BPA oxidation reactions are considered to be cost-effective and environmentally-sustainable procedures (Tsai et al., 2009; Chiang et al., 2004), which could combine heavy metal reduction with organic pollutants oxidation to achieve effective utilization of photo-generated electrons and holes (Zhang et al., 2018a; Liu et al., 2007).

In recent decades, MOFs (metal-organic frameworks) have arose extensive interests in photocatalysis, due to that the organic ligands or metal ions/clusters can capture light to generate photo-induced electrons and holes (Aguila et al., 2018). MOFs as effective photocatalysts have been used for CO_2 reduction (Chen et al., 2016), hydrogen generation via water splitting (Karthik et al., 2018; Song et al., 2017), organic pollutants degradation (Zhang and Wang, 2017) and Cr(VI) reduction (Du et al., 2019a, b; Wang et al., 2019a). To further promote the photocatalytic performances of MOFs, many attempts have been taken to combine MOFs with some semiconductor photocatalysts to promote the separation of photo-induced charge carriers and the water stability (nulla). For example, Wang and coworkers fabricated series MOFs/semiconductors composites (like BUC-21/$Bi_{24}O_{31}Br_{10}$, BUC-21/g-C_3N_4, g-C_3N_4/UiO-66, UiO-66-NH_2/Ag_2CO_3) along with MOFs/conductive organic polymers (like PANI/MIL-100(Fe) heterojunctions) to achieve enhanced photocatalytic Cr(VI) reduction, photocatalytic oxidation of organic pollutants, and photo-Fenton degradation toward organic pollutants (Du et al., 2019a; Zhou et al., 2019; Zhao et al., 2019; Yi et al., 2019a; Chen et al., 2020).

As a most widely explored semiconductor photocatalyst, TiO_2 displays good photocatalytic performances (Ohko et al., 2001; Lee and Park, 2013). Also, TiO_2 is deemed to be non-toxic, chemically and biologically stable, along with relatively inexpensive (Subagio et al., 2010; Zhao et al., 2019). However, some disadvantages like large bandgap energy, rapid recombination of photo-generated electrons and holes, and lower solar light utilization efficiency limited TiO_2's application in water treatment (Ohno et al., 2004). Some strategies like doping TiO_2 with metallic elements (Pt, Co, Cu) (Iwasaki et al., 2000; Irie et al., 2009; Kim et al., 2005), non-metallic elements (S, N, C, F) (Ohno et al., 2004; Xing et al., 2009; Li et al., 2005) or inorganic semiconductor (CdS, BiOI, WO_x) (Gao et al., 2012; Li et al., 2001; Zhang et al., 2009) were adopted to overcome the disadvantages of TiO_2. As well, various methods have been used to inhibit the reintegration of electron-hole pairs or expand the absorbable light region (Li et al., 2001; Seh et al., 2012; Luo et al., 2019). Among them, sulfur-doped TiO_2 (S-TiO_2) displayed outstanding photocatalytic decomposition performances toward methylene blue, 4-chlorophenol and tetracycline under visible light (Ohno et al., 2004; Wang et al., 2011; Ho et al., 2006).

In this study, S-TiO_2/UiO-66-NH_2 composites were facilely constructed from S-TiO_2 and UiO-66-NH_2 via ball-milling, which were further used as photocatalysts to achieve efficient Cr(VI) reduction and BPA oxidation under low-power visible light provided by LED. Furthermore, the cycle experiments were carried out to confirm the stability and reusability of S-TiO_2/UiO-66-NH_2 composites. The probable reaction mechanism for the improved photocatalytic activities was also proposed and confirmed.

2. Experimental

2.1. Materials and characterization

The used chemicals, the characterization instruments and electrochemical tests were put into the supplementary information.

2.2. Synthesis of S-TiO$_2$

37.0 mL anhydrous ethanol and 1.0 mL nitric acid were mixed and stirred for 10 min. Then, 2.0 mL tetrabutyl titanate was dropped into the solution and stirred for another 20 min. After that, thioacetamide was added with the S/Ti ratio of 1:10. After stirring for 15 min, the suspension was sealed in the Teflon-lined autoclave for solvothermal treatment at 190 ℃ for 12 h. Finally, the S-TiO_2 was obtained after filtration, washing and drying under vacuum at 100 ℃ for 4 h (Wang et al., 2008).

2.3. Preparation of S-TiO$_2$/UiO-66-NH$_2$

The UiO-66-NH_2 was synthesized following the previous reported procedure (Xu et al., 2018). The S-TiO_2/UiO-66-NH_2 composites were synthesized by ball grinding (30 Hz, 20 min). A series of composites, referred as U1T*x* (the letters "U" represents "UiO-66-NH_2", "T" represents "S-TiO_2", and "*x*" represents mass ratio), were obtained by adding S-TiO_2 and UiO-66-NH_2 with different mass ratios into the ball mill tank (Scheme 1).

2.4. Photocatalytic activity test

Photocatalytic reduction of Cr(VI) was conducted in Cr(VI) (as the form of $K_2Cr_2O_7$) aqueous solution with initial volume of 50.0 mL and initial concentration of 5.0 mg L^{-1}, in which the dosage of photocatalyst was 10.0 mg and the pH values were adjusted to 2.0–8.0 by H_2SO_4 or NaOH solutions with suitable concentrations. All the experiments were carried out at room temperature (25 ℃). After reaching adsorption-desorption equilibrium after adsorption in dark for 60 min, the suspensions under magnetic stirring (180 r/min) were irradiated under visible light provided by an LED with optical power of 50 mW (Beijing perfectlight technology Co. Ltd), and the spectra of visible light was depicted in Fig. S1. The 1.5 mL aliquots were extracted at designed time intervals and filtered with 0.22 μm PTFE membrane. Finally, the residual Cr(VI) concentration was measured by the diphenylcarbazide colorimetric method (Scheme. S1).

The photocatalytic BPA degradation performances of U1T*x* photocatalysts was also studied. The photocatalytic BPA degradation experiment was similar to that of Cr(VI) reduction, except that the Cr(VI) solution was replaced with BPA aqueous solution. The rudimental

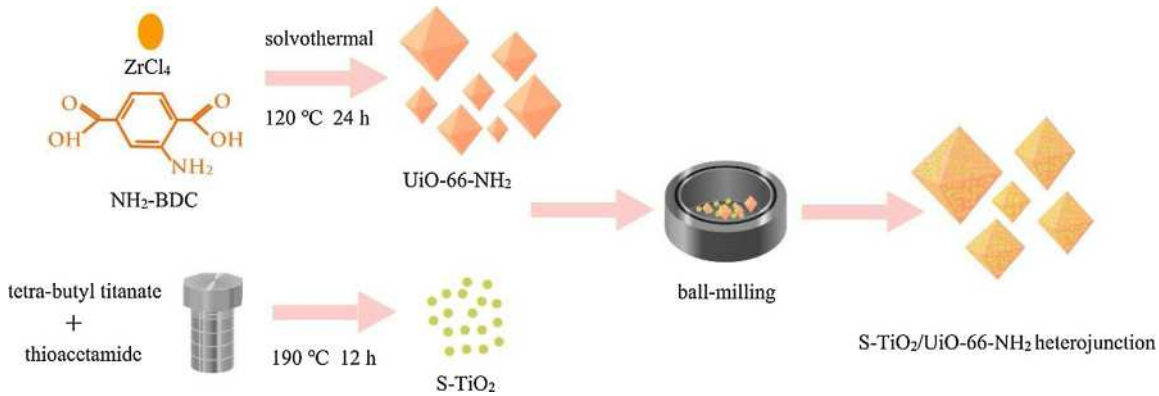

Scheme 1. Synthetic illustration for the preparation of S-TiO_2/UiO-66-NH_2 composites.

content of BPA was measured by high performance liquid chromatograph (HPLC) (LC-20AT, SHIMADZU Co. Ltd), in which UV detectors is equipped and the target analytes are separated by C18 column (5 μm, 2.1 mm × 250 mm) (Cariot et al., 2012).

The apparent quantum efficiency (AQE) experiments were carried out under light of different wavelengths using 300 W Xe lamp with the aid of different filters, and the results were obtained according to the removal amount of pollutants. The AQE for Cr(VI) reduction followed Eq. (1), and the calculation of incident photons followed the Eq. (2) (Li et al., 2019a; Velegraki et al., 2018).

$$\mathrm{AQE(Cr)} = \frac{3\times[\text{number of reduced Cr(VI)}]}{\text{number of incident photons}} \tag{1}$$

$$N_P^i = \frac{Pt\bar{\lambda}}{hc} \tag{2}$$

Where, P is the optical power, t is the irradiation time, λ is wavelength of light, and h and c are Planck constant (h = 6.62607015 × 10^{-34} J·s) and lightspeed (299,792,458 m s^{-1}), respectively.

3. Results and discussion

3.1. Material characterizations

The PXRD patterns of the as-prepared UiO-66-NH_2 matched well with that reported in the literature and simulated one (Fig. S7), demonstrating that pure UiO-66-NH_2 was synthesized successfully (Xu et al., 2018). As Fig. 1a, the characteristic peaks at 25.2°, 37.8°, 47.9°, 53.8°, 55.0°, 62.5°, 70.2° and 74.8° were attributed to S-TiO_2 (anatase) (PDF#99 − 000-0105), in which the typical peaks at 2θ = 25.2°, 37.8°, 47.9°, 55.0°, 62.5° could be indexed to (101), (004), (200), (211) and (204) lattice planes of S-TiO_2 anatase (Wang et al., 2009; Arconada et al., 2009). The PXRD peaks of U1Tx composites matched well with the typical peaks of UiO-66-NH_2 and S-TiO_2. The typical peaks at 7.5° and 8.7° of UiO-66-NH_2 maintained well with decreasing intensity as increasing mass content of S-TiO_2. In FTIR spectra (Fig. 1b), the characteristic peaks at 600 - 800 cm^{-1} were ascribed to Zr-O_2 cluster (Yang et al., 2015), which became weaker with the decrease of UiO-66-NH_2 content in U1Tx composites. It was observed that the peaks at 1432 cm^{-1} and 1387 cm^{-1} corresponded to the carboxylic groups stretching in NH_2-BDC ligands (Xu et al., 2018). The peak at 1632 cm^{-1} of S-TiO_2 spectrum could be the O−H bond bending vibrations of adsorbed water molecules (Coronado et al., 2003; Su et al., 2012).

In order to further confirm the successful fabrication, the chemical compositions and states on the surface of S-TiO_2, UiO-66-NH_2 and U1T3 were investigated with XPS determination (Fig. 1c). The XPS survey scan spectra of S-TiO_2 displayed the S 2p and Ti 2p characteristic peaks, indicating that sulfur was successfully doped in S-TiO_2. The S 2p peaks at 168.7 eV and 169.9 eV were attributed to $2p_{3/2}$ and $2p_{1/2}$, demonstrating that S^{6+} existed as chemisorbed SO_4^{2-} species in the lattice (Wang et al., 2018). Therefore, Ti^{4+} ions were substituted by S^{6+} cations to form Ti − O− S bond, leading to the promoted visible light absorption (Ma et al., 2014; Huo et al., 2016). The successful doping of S element into TiO_2 was confirmed by the determination of the sulfur content in S-TiO_2 and U1Tx composites (like U1T3), which revealed the sulfur content percentages in S-TiO_2 and U1T3 were 1.27 wt.% and 1.04 wt.%, respectively (Table S2). The observed Zr 3d peaks of UiO-66-NH_2 at 182.9 eV and 185.3 eV corresponded to Zr $3d_{5/2}$ and Zr $3d_{3/2}$, confirming the presence of Zr-O clusters (Xu et al., 2018). The XPS results exhibited the obvious Ti 2p and Zr 3d peaks of composites (like U1T3) that were originated from S-TiO_2 and UiO-66-NH_2, respectively. It could be noted that the binding energies of Ti 2p were shifted from a higher binding energy at 464.5 eV and 458.8 eV to lower binding energy at 464.3 eV and 458.6 eV (Fig. 1d), implying that a higher electron density was on the surface of Ti and electron transfer from UiO-66-NH_2 to S-TiO_2 due to their successfully combination (Yi et al., 2019a; Bai et al., 2015).

The TGA results illustrated that the weight loss of the U1Tx decreased with the increase of S-TiO_2, in which the weight losses were consistent with the organic ligand (BDC-NH_2 ligands) loss of UiO-66-NH_2 in different mass proportions of the U1Tx composites (Fig. S8). Thus, it can be further affirmed the formation of S-TiO_2/UiO-66-NH_2 (U1Tx) composites.

The SEM and TEM images were depicted in Fig. 2, in which the pristine UiO-66-NH_2 exhibited smooth regular octahedron with particle size ranging from 600 nm to 2000 nm and the S-TiO_2 nanoparticles sizes were ca. 20 nm. It can be clearly seen that the surface of UiO-66-NH_2 were wrapped by S-TiO_2 nanoparticles after the ball-milling process (like U1T3). The SEM-EDS (Fig. 3) revealed the uniform distribution of N and Zr (the specific element of UiO-66-NH_2), S and Ti (the representative element of S-TiO_2) elements, which further verified the fabrication of UiO-66-NH_2 and S-TiO_2 into composites. The selected area electron diffractograms (SAED) pattern for U1T3 was illustrated in Fig. 4b (inset). The diffraction rings (from the center) demonstrated the lattice fringes of 3.53 Å, 2.38 Å, 1.90 Å and1.67 Å, corresponding to the (101), (004), (200) and (211) lattice plane of TiO_2 (PDF#99 − 000-0105 standard card) (Subramanian et al., 2006). HRTEM results also displayed the lattice structure and outline of the U1T3 composite (Fig. 4), in which the calculated lattice fringe was 0.352 nm, corresponding to the (101) lattice plane of anatase TiO_2 (Gao et al., 2012).

The UV–vis DRS spectra (Fig. 5a and b) demonstrated the optical absorption property of the UiO-66-NH_2, S-TiO_2 and their composites. The band gap (E_g) values of U1T1, U1T2, U1T3 and U1T4 were estimated as 2.79 eV, 2.78 eV, 2.75 eV and 2.75 eV by using Eq. (3) (Du et al., 2019a; Yi et al., 2019a), indicating that the series U1Tx composites could be excited by visible light. As well, it can be found that the light absorption behaviors of U1Tx were similar to that of S-TiO_2.

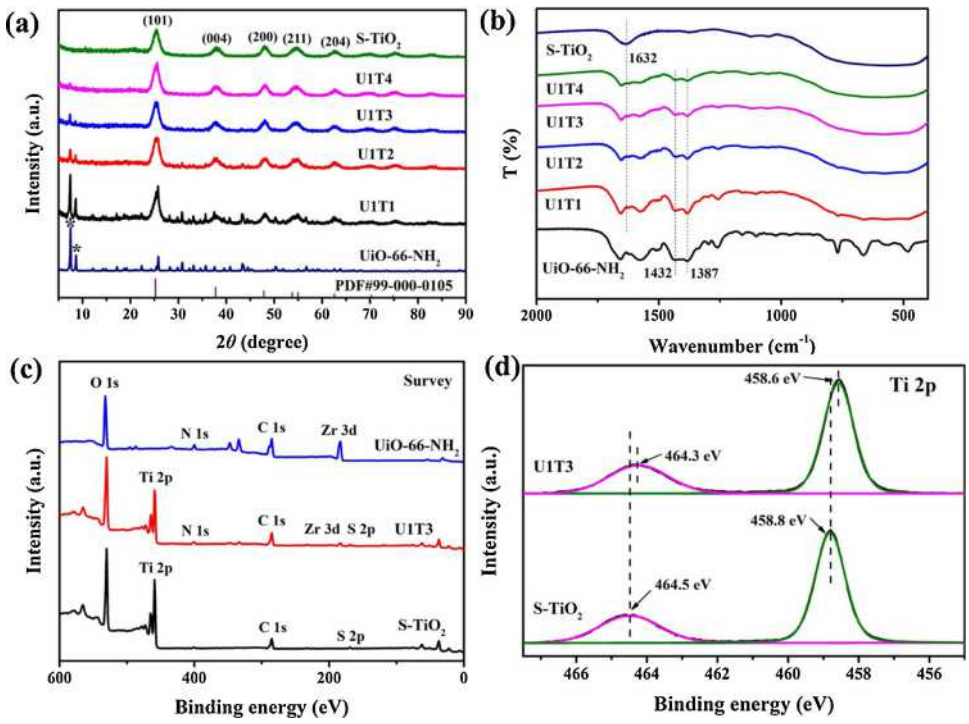

Fig. 1. PXRD patterns (a), FTIR spectra (b) and XPS spectra of S-TiO_2, UiO-66-NH_2 and U1T3: survey scan (c), Ti 2p (d). (PDF#99-000-0105: PDF standard card of anatase TiO_2, *Stars* (*) represent the characteristic peaks of UiO-66-NH_2).

$$\alpha h\upsilon = A(h\upsilon - Eg)^{n/2} \quad (3)$$

Where, α is the diffuse absorption coefficient, ν is the incident photon frequency, h is the light constant, and n is decided by type of the semiconductor (indirect (n = 4)).

The Mott–Schottky measurements of S-TiO_2 and UiO-66-NH_2 were also conducted to determine the conduction band (CB) values (Fig. 5c and d). The slope of C^2 value versus potential was positive, proving that the UiO-66-NH_2 and S-TiO_2 were both the n-type semiconductors (Yi et al., 2019a; Rammelt et al., 2001). It was observed that the CB of UiO-66-NH_2 and S-TiO_2 were ca. −0.80 eV and -0.55 eV *versus* the Ag/AgCl electrode at pH = 7.0, respectively, matching well with the previous reports (Du et al., 2019b; Zhao et al., 2016). The valence band (VB) potential values were calculated as 2.30 eV and 2.84 eV *vs*. NHE (E_{CB} = E_{VB} - E_g) (Zou et al., 2016) based on the estimated band gaps.

3.2. Photocatalytic activity

3.2.1. Photocatalytic Cr(VI) reduction activities of U1Tx

The photocatalytic reduction experiments of the prepared materials were carried out under LED visible light (Fig. 6a). After the adsorption in dark, all U1T*x* composites exhibited higher photocatalytic efficiencies than the individual UiO-66-NH_2 and S-TiO_2. In detail, U1T3 showed the highest removal efficiency (94.9 % at 45 min, 100.0 % within 75 min), and followed by U1T2 (93.4 % at 45 min, 100.0 % within 75 min), U1T4 (94.2 % at 45 min, 100.0 % within 75 min) and U1T1 (81.7 % at 45 min, 97.8 % within 75 min). In addition, photocatalytic Cr(VI) reduction conformed to the pseudo-first order model (ln (C/C_0) = kt), in which k represented the apparent rate constant (min^{-1}). The Cr(VI) reduction activities of series composites exhibited saddle-shaped curve, and the k values followed the order of U1T3 > U1T2 > U1T4 > U1T1 > S-TiO_2 > UiO-66-NH_2 (Fig. 6b). The Cr(VI) removal efficiency over U1T3 was 30.0 % within 150 min without the presence of light, demonstrating that the efficient Cr(VI) removal was assigned to the photocatalytic process with the presence of both U1T3 as photocatalyst and visible light rather than catalytic reaction over U1T3.

The apparent quantum efficiency (AQE) is a critical index to evaluate photocatalytic activities (Li et al., 2019b). As demonstrated in Fig. 6c, The AQEs of U1T3 achieved 0.56 %, 0.48 %, 0.33 %, 0.05 % and 0.04 % at 315 nm, 330 nm, 365 nm, 380 nm, 400 nm and 420 nm, respectively. The AQEs at different wavelengths were well corresponded to the curve trend of UV–vis DRS spectra, confirming that the Cr(VI) removal over U1T3 was a photo-induced photocatalysis process (Bai et al., 2017; Zhang and Park, 2019).

The BET specific surface area results were in Table S3 and Fig. S10. It was worthy to note that the increasing introduction of S-TiO_2 led to the decreasing surface areas of composites from 341.14 $m^2\ g^{-1}$ to 154.26 $m^2\ g^{-1}$. Generally, the larger specific surface areas could lead to more exposure of active sites, which can facilitate the photocatalytic activities by promoting charge transfer and effective utilization of visible light (Yi et al., 2019a; Chen et al., 2007). However, the excessive introduction of S-TiO_2 might be detrimental to the formation of an effective heterogeneous interface, resulting in the declined efficiency of charge transfer (Liu et al., 2016). U1T3 was selected for the subsequent investigation of influences resulted from pH and co-existing ions, considering its highest photocatalytic efficiency (Du et al., 2019a).

Previous studies have shown that the pH values have significant effect on the Cr(VI) reduction rate (Wang et al., 2016a). Generally, the lower pH values could contribute to photocatalytic Cr(VI) reduction (Shi et al., 2011; Yoon et al., 2009). However, when pH values were 2.0 and 3.0, the photocatalytic Cr(VI) reduction efficiencies were lower than that at pH = 4.0 (Fig. 7a). It has been reported that the pH values of solutions could influence the surface potential of the photocatalyst (Grover et al., 2013). As shown in Fig. 7b, the zeta potentials were positive at pH = 2.0 and 3.0, which facilitated the adsorption of Cr(VI) primarily in forms of $HCrO_4^-$ or $Cr_2O_7^{2-}$ under acid conditions (Guo et al., 2019). Nevertheless, the excessive Cr(VI) adsorption might block the photoactive sites to inhibit the further Cr(VI) reduction. When 3.0 < pH < 7.0, the photocatalytic reaction process follows the Eq.s (4) and (5), and lower pH value (pH = 4.0) favored Cr(VI) reduction due to the abundant H^+ (Du et al., 2019a; Yi et al., 2019b). Under alkaline environment, the dominating Cr(VI) specie is CrO_4^{2-} (Wang et al.,

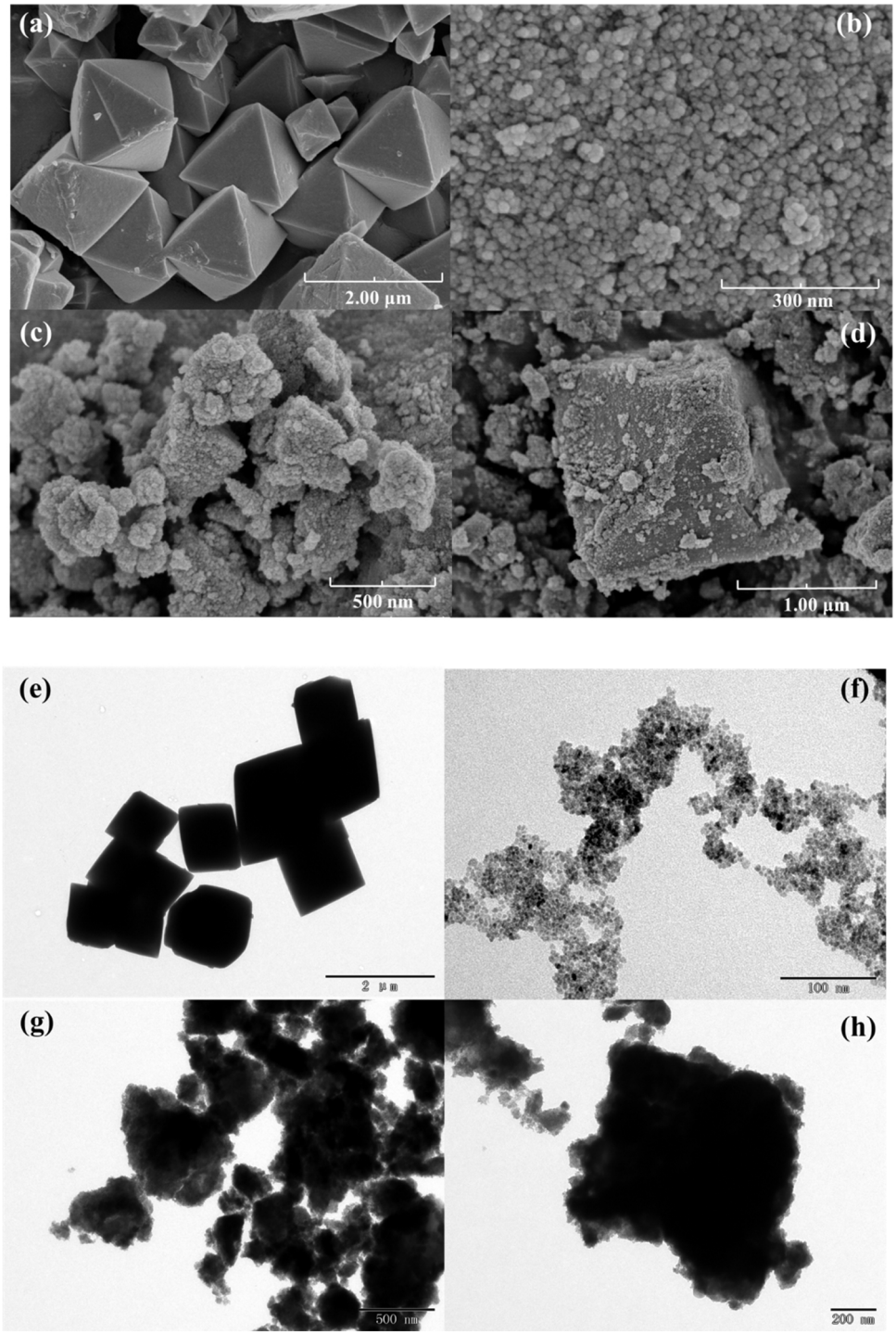

Fig. 2. The SEM and TEM images of UiO-66-NH_2 (a, e), S-TiO_2 (b, f) and U1T3 (c, d, g, h).

2016a), leading to a reaction as expressed in Eq.s (5) and (6). The efficiency of Cr(VI) removal decreased obviously at pH = 8.0, and it could be attributed to poor Cr(VI) adsorption resulting from weak electrostatic attraction between the chromate anion and the negatively charged surface of U1T3 as well as the formed $Cr(OH)_3$ precipitates which might cover the active sites of U1T3 (Li et al., 2019a).

$$14H^+ + Cr_2O_7^{2-} + 6e- \rightarrow 2Cr^{3+} + 7H_2O \quad (4)$$

$$2H_2O + 2h^+ \rightarrow H_2O_2 + 2H^+ \quad (5)$$

$$CrO_4^{2-} + 4H_2O + 3e^- \rightarrow Cr(OH)_3(s) + 5OH^- \quad (6)$$

Under the light irradiation, the photoinduced electron and hole could be produced. It was found that ethanol could capture photo-induced holes (Liu et al., 2011), and Cr(VI) reduction efficiency can be also photochemically promoted in absence of catalysts (Machado et al., 2014), which could enhance the photocatalytic Cr(VI) reduction. The influence of different ethanol dosage on Cr(VI) reduction were investigated (Fig. 7c). With the increase of ethanol, U1T3 obtained the higher efficiencies of photocatalytic Cr(VI) reduction, and k value increased from 0.067 min^{-1} (0.05 mL ethanol) to 0.1674 min^{-1} (0.5 mL ethanol) (Fig. 7d).

According to the previous reports (Li et al., 2019a; Wang et al.,

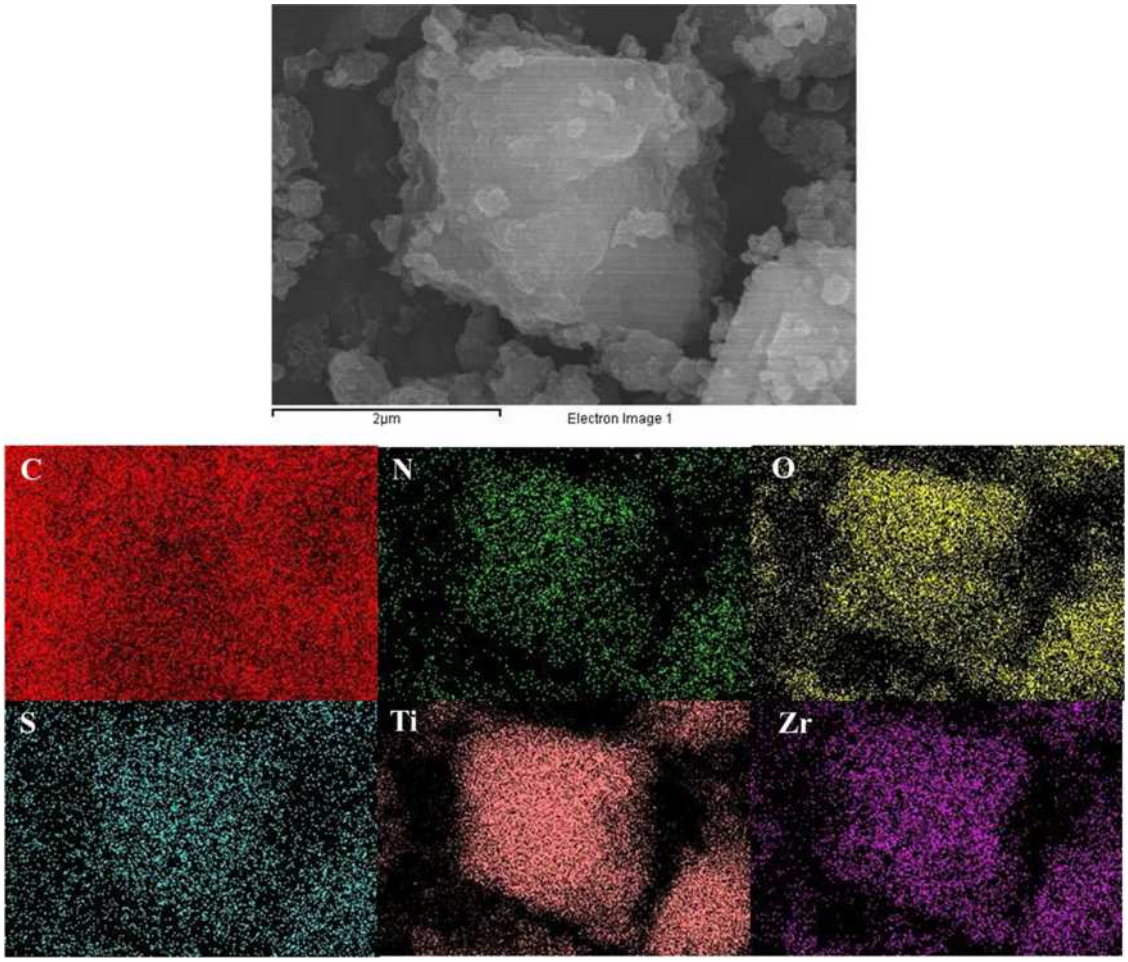

Fig. 3. The EDS mapping images of U1T3 composite.

2000), the coexisting ions like inorganic ions and organic matters could have an effect on photocatalytic performances. The Cr(VI) aqueous solution was prepared from real lake water and tap water (Table S4) to confirm the effect of foreign ions (Fig. 9a). It was demonstrated that the Cr(VI) removal efficiencies in lake water and tap water were 86.8 %, 87.1 %, respectively. The photocatalytic rate k values of lake water (0.0287 min^{-1}) and tap water (0.0259 min^{-1}) were demonstrated in Fig. 9b. Similar to the reported literatures (Li et al., 2019a; Yi et al., 2019b), the decrease of Cr(VI) reduction efficiency was ascribed to the negative effect of inorganic ions in the water. It could be observed that the photocatalytic efficiencies in lake water was higher than that in tap water, which resulted from the positive impact of organic matters that consumed the photo-induced holes (Yin et al., 2018; Li et al., 2010) as well as achieved photochemical Cr(VI) reduction (Machado et al., 2014).

The influences of the coexisting matters on photocatalytic process

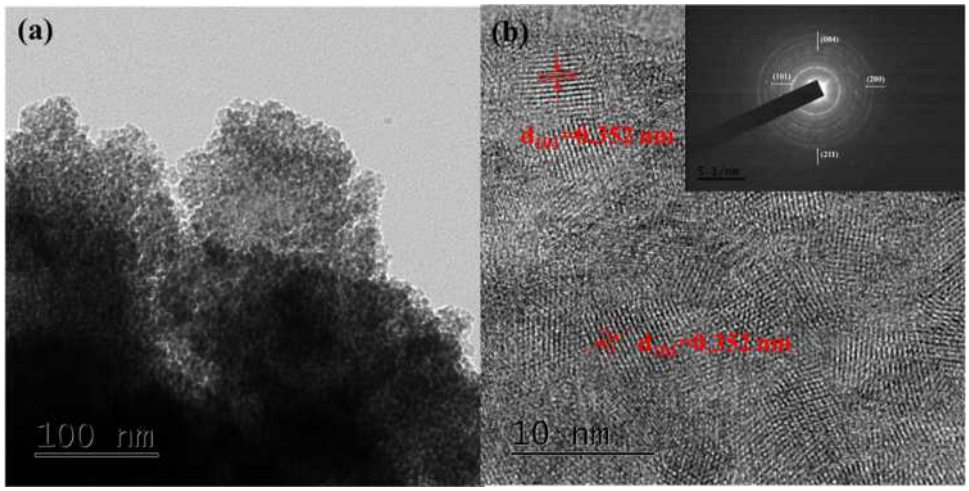

Fig. 4. The HRTEM and SAED images of U1T3 composite.

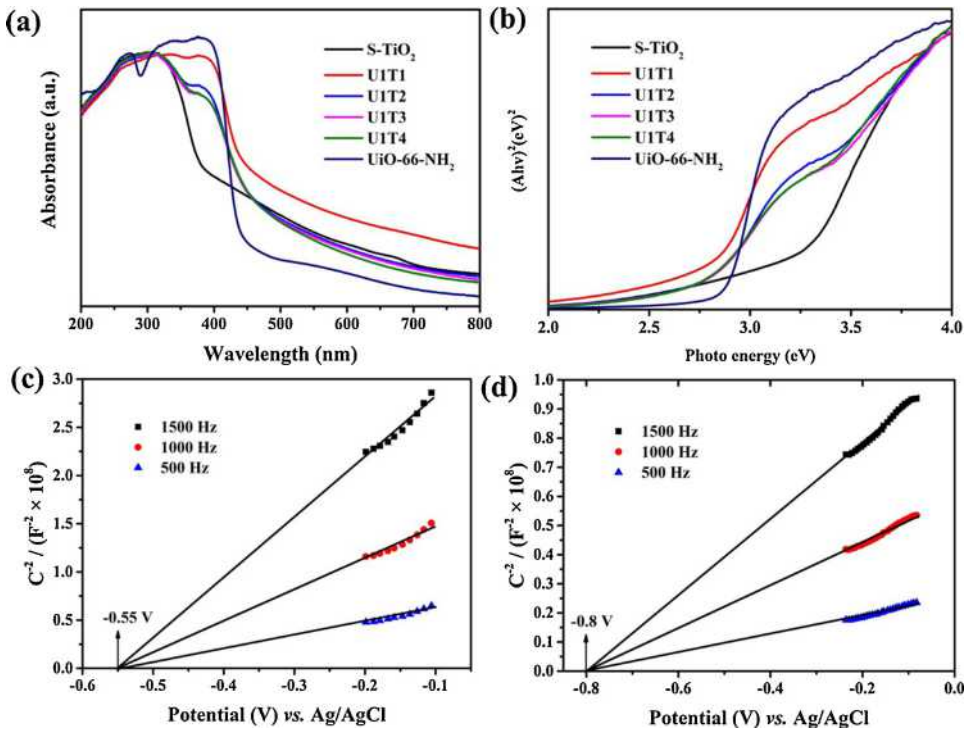

Fig. 5. The UV–vis DRS (a) and *Eg* plots (b) of the UiO-66-NH_2, S-TiO_2 and U1T*x*. Mott-Schottky curves of S-TiO_2 (c) and UiO-66-NH_2 (d).

was further verified by the Box-Behnken experimental design methodology. Generally speaking, some inorganic cations like Na^+, K^+, Ca^{2+} and Mg^{2+} cannot exert significant impacts on the photocatalytic process (Yi et al., 2019a; Wang et al., 2012), because the photo-generated electrons or holes were hardly utilized by them due to the stability and high oxidation state. Therefore, only the inorganic anions like Cl^- (A), NO_3- (B) and SO_4^{2-} (C) along with DOM (D) were selected as experimental variables to explore photocatalytic efficiencies of Cr(VI) reduction under LED visible light. The series designed experiments (29 runs) were shown in Table. S5. The results indicated that the response (photocatalytic efficiency %) and variables conformed to the quadratic polynomial model (Eq. (7))

$$\text{Efficiency}\,\% = 88.34 - 2.97A - 0.60B - 0.46C + 6.60D - 2.81AB - 0.52AC + 2.36AD - 2.63BC - 1.42BD + 1.10CD - 3.94A^2 - 1.89B^2 - 4.39C^2 + 0.031D^2 \quad (7)$$

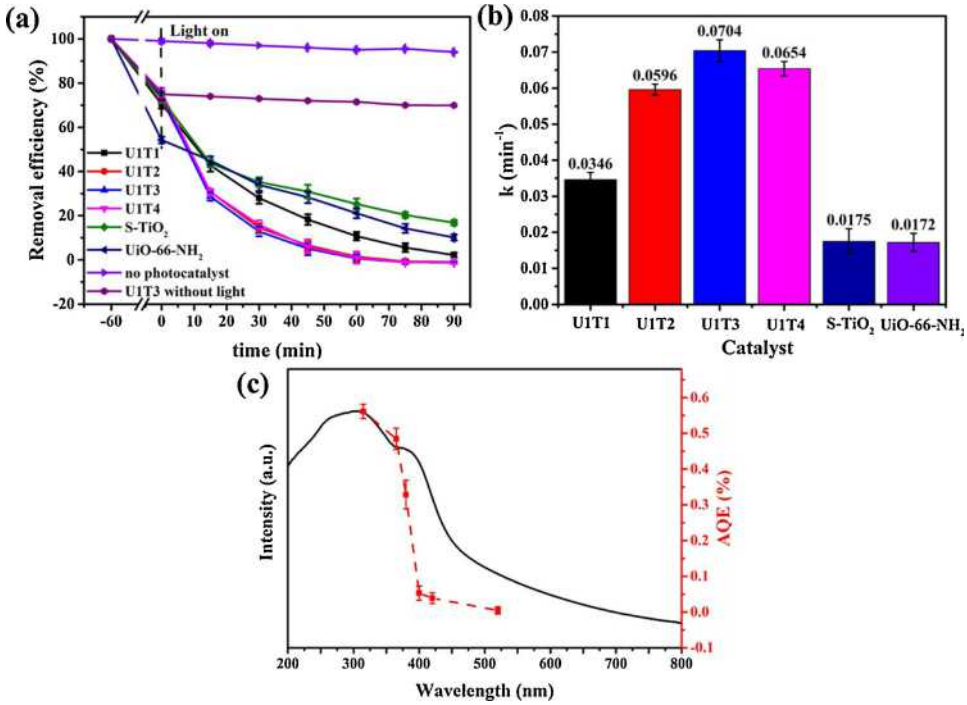

Fig. 6. Photocatalytic Cr(VI) degradation (a) and comparison of rate constant *k* (b) over UiO-66-NH_2, S-TiO_2 and U1T*x* (x = 1, 2, 3, 4) hybrids. AQE results of Cr(VI) reduction under different monochromatic light (c). Conditions: 10.0 mg (200 mg L^{-1}) of U1T3, Cr(VI) =5.0 mg L^{-1}, 50 mL, pH = 4.0.

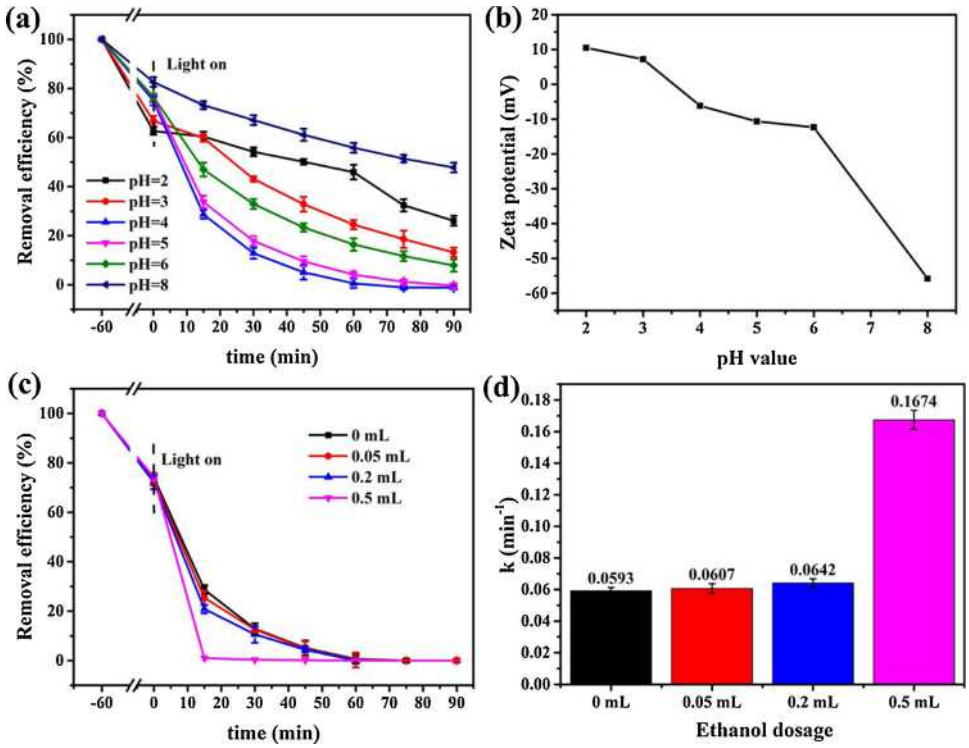

Fig. 7. (a) Influence of pH values over U1T3 on Cr(VI) reduction. (b) The zeta potential of U1T3. Effect of different ethanol concentrations over U1T3 on Cr(VI) reduction (c) and rate constant k (d), pH = 4.0.

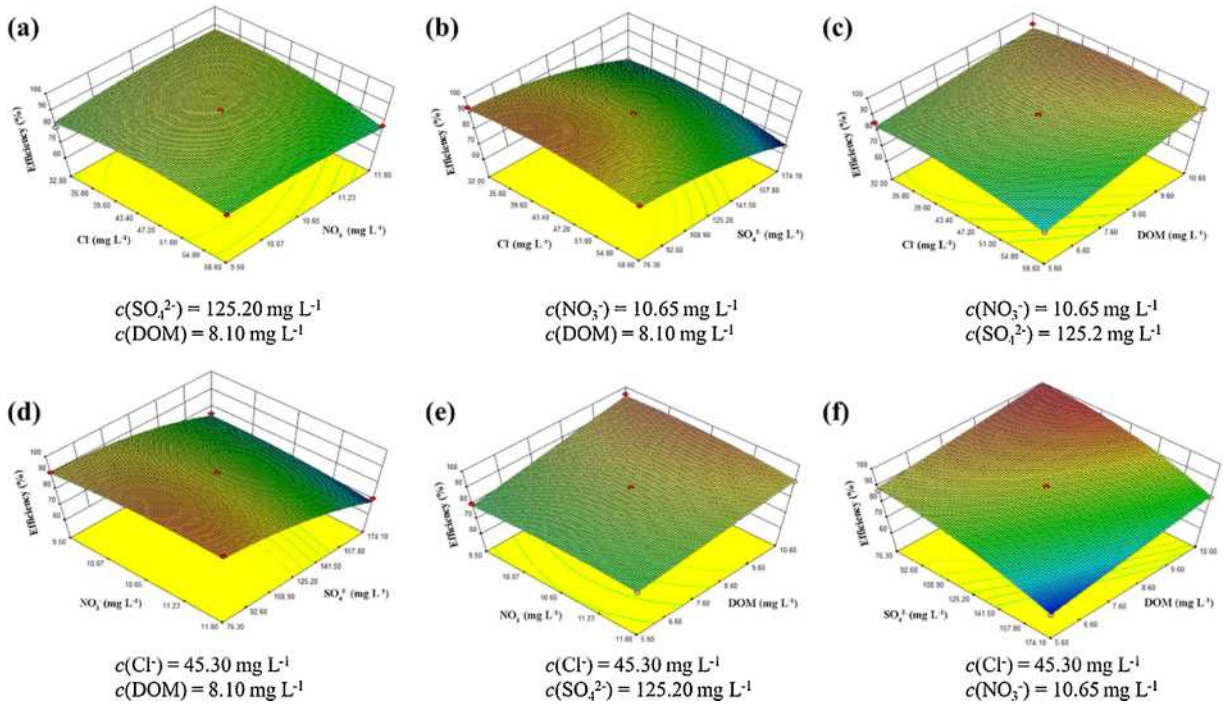

Fig. 8. Response surface diagram of the effect of foreign ions on photocatalytic reduction efficiency of Cr(VI) over U1T3.

According to the ANOVA results of photocatalytic efficiencies, the R^2 and adjusted R^2 were calculated as 0.9807 and 0.9615, respectively, indicating that the model possessed a high significance. Besides, the F values were 416.26, 165.64, 33.64, 1.39 for SO_4^{2-}, DOM, Cl- and NO_3-, respectively, demonstrating that SO_4^{2-} and DOM can exert obvious impact on photocatalytic Cr(VI) reduction, followed by Cl- and NO_3-. As shown in the three-dimensional surface plots (Fig. 8), the inorganic anions especially SO_4^{2-} could heavily inhibit Cr(VI) reduction, as SO_4^{2-} ions can be adsorbed onto U1T3 resulting from the electronic interactions (Yi et al., 2019a). With the increase of DOM concentrations, the Cr(VI) removal efficiencies were enhanced, indicating that DOM posed a positive impact on Cr(VI) reduction. Therefore, it could be concluded that inorganic ions had a negative effect on photocatalytic Cr(VI) reduction, while DOM could promote the reduction efficiencies of U1T3 photocatalyst.

Considering that S-TiO_2 and UiO-66-NH_2 (U1T3) could achieve

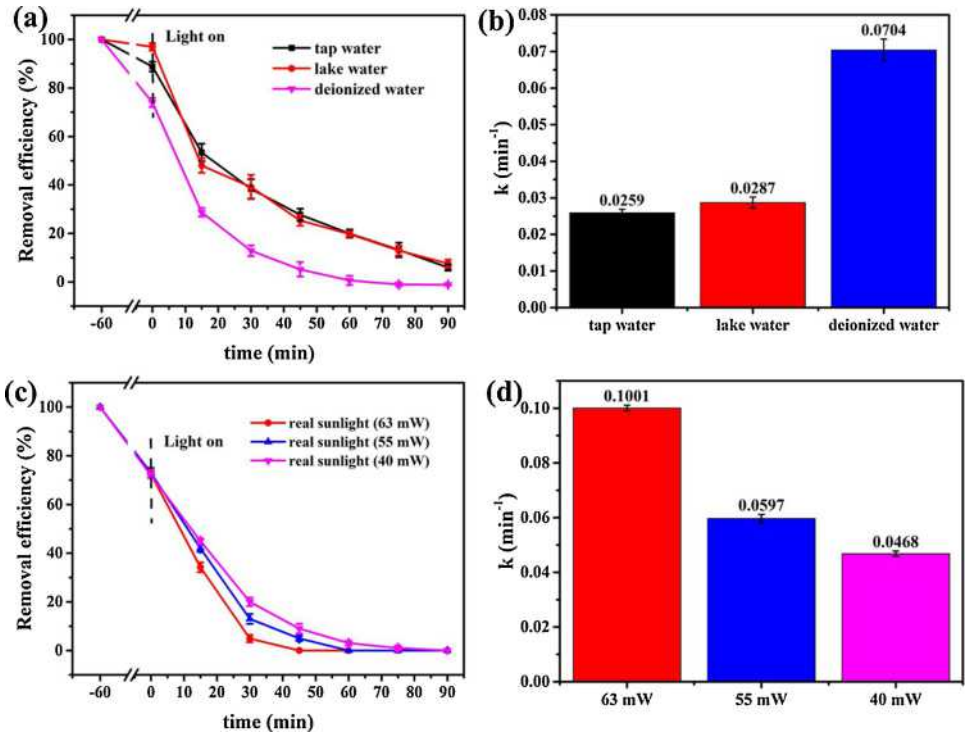

Fig. 9. Effect of foreign ions on Cr(VI) reduction (a) and rate constant *k* (b). Performances of Cr(VI) removal under real sunlight (d) and rate constant *k* (d). Conditions: 10 mg of U1T3, Cr(VI) =5 mg L^{-1}, 50 mL, pH = 4.0.

good photocatalytic performances under low-power visible light, it might possess preferable photocatalytic activities under real sunlight irradiation. In this study, the experiments were conducted under real sunlight at Daxing campus of BUCEA (39°44′ N, 116°17′E) on December 11th (15 °C), 12th (15 °C) and 13th (13 °C). The average optical powers were 63 mW, 55 mW and 40 mW, respectively. As shown in 9c, the photocatalytic efficiencies decreased as the optical power reduced and the *k* values were determined to be 0.1001 min^{-1}, 0.0597 min^{-1} and 0.0468 min^{-1} (Fig. 9 d). It was worth noting that the correlation between the actual sunshine intensity and *k* value was positive, indicating that the optical power was one of the influence factors of photocatalytic Cr(VI) reduction. Additionally, comparing with the photocatalytic performances under LED visible light, U1T3 exhibited higher efficiencies under real sunlight when the optical power was 63 mW.

3.2.2. Photocatalytic bisphenol A degradation

Besides Cr(VI) reduction, the photocatalytic oxidative degradation toward BPA over U1T3 was also studied. As described in Fig. 10a, the BPA degradation efficiency was only 4.0 % under the LED visible light irradiation without any photocatalyst. In the presence of pristine S-TiO_2 and UiO-66-NH_2, BPA was degraded with removal efficiencies of 89.1 % and 16.2 % within 120 min under LED visible light. In comparison, BPA degradation efficiency over U1T3 achieved up to 97.4 %, which was higher than that with P25 as photocatalyst. The influences of different pH values ranging from 3.0–10.0 were also investigated. It was found in Fig. 10b that U1T3 exhibited good performances toward BPA degradation and there was only 5.0 % difference between pH = 3.0 and pH = 10.0. In particular, BPA degradation efficiency achieved 97.5 % with highest degradation rate (0.0298 min^{-1}) at pH = 6.0 (Fig. S15), indicating that photocatalytic BPA degradation preferred to be carried out under neutral conditions.

In order to further explore the potential photocatalytic performances of simultaneous reduction and oxidation, experiment was conducted to investigate U1T3′s photocatalytic activity in the Cr(VI)/BPA matrix. As illustrated in Fig. 10c, photocatalytic Cr(VI) reduction and BPA oxidation efficiencies achieved 100.0 % and 97.4 % over U1T3 under LED visible light within 120 min in the mono-component system, respectively. In the mixture of Cr(VI) and BPA solution, the Cr(VI) removal efficiency was sustained as 100.0 % with decreasing photocatalytic reduction rate from 0.0704 min^{-1} (Cr(VI) solution) to 0.0220 min^{-1} (Cr(VI)/BPA matrix) (Fig. 10d), and the photocatalytic efficiencies of BPA degradation declined slightly to 90.8 %. The results revealed that U1T3 maintained good performances for Cr(VI) reduction and BPA degradation when Cr(VI) and organic pollutant existed simultaneously.

The generated intermediate products in the process of photocatalytic BPA degradation within 120 min were detected by LC–MS (Table. S9). Several intermediate compounds like 4-isopropylphenol (*m/z* = 135), hydroquinone (*m/z* = 109), p-benzoquinone (*m/z* = 108), 4-isopropylenecatechol (*m/z* = 149), 4-isopropenylphenol (*m/z* = 133), and phenol (*m/z* = 93) were identified and confirmed by both MS determination and the previous reports (Subagio et al., 2010; Molkenthin et al., 2013; Li et al., 2019c). According to the present experimental data and the literatures (Chiang et al., 2004; Lu et al., 2013; Sharma et al., 2015), the possible pathway of photocatalytic BPA degradation under visible light was proposed as Fig. 11. The electron-rich C4 of BPA was firstly attacked, followed by the formation of 4-isopropylphenol and phenol (Li et al., 2019c). As the reaction continues, series intermediates were formed. When the reaction time was prolonged, it was believed that the BPA could be completely mineralized into CO_2 and H_2O. It can be concluded that U1T3 exhibited preferable photocatalytic performances toward Cr(VI) reduction and BPA oxidation under LED visible light, which can exceed most counterparts as listed in Table 1.

3.2.3. Reusability and stability of U1T3

It is of great importance to investigate the reusability and stability of U1T3 for practical application. As depicted in Fig. 12a, U1T3 showed preferable photocatalytic performance for Cr(VI) reduction. The performances of photocatalyst only have a slight decrease after two runs. In the 4th cycle, the Cr(VI) removal efficiency decreased to 85.0 % due to the adsorption of Cr(III) or Cr(VI) ions on the surface of catalyst. The

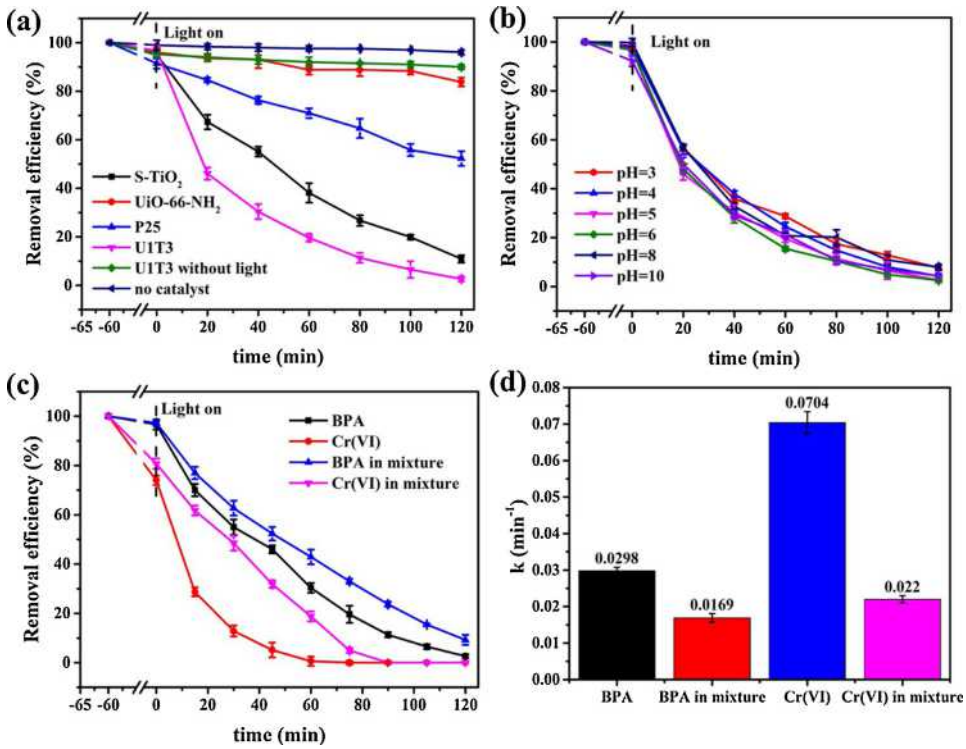

Fig. 10. Photocatalytic BPA degradation performances of different photocatalysts (a) and influences of pH values on BPA degradation (b). Effect of organic pollutant BPA on Cr(VI) reduction (c) and rate constant *k* (d). Conditions: 10.0 mg of U1T3, BPA =5.0 mg L^{-1}, 50 mL.

survey XPS spectra (Fig. 12b) after photocatalysis confirmed the presence of Cr element. As shown in Fig. 12c, the XPS spectrum of Cr 2p could be curve fitted with three peaks at 577.2, 580.2 and 586.8 eV. The peaks at 577.2 and 580.2 eV were attributed to Cr $2p_{3/2}$ while that at 586.8 eV was attributed to Cr $2p_{1/2}$. It was worth noting that the observed peaks at 580.2 eV and 586.8 eV were assigned to Cr(VI) and the peak at 577.2 eV was regarded the signals of Cr(III) (Zhao et al., 2014).

For comparison, the cycle experiments of S-TiO_2 and UiO-66-NH_2 were also conducted. It was demonstrated that both UiO-66-NH_2 and S-TiO_2 exhibited inferior photocatalytic efficiencies. Cr(VI) removal activities over S-TiO_2 and UiO-66-NH_2 accomplished 81.5 % and 76.1 % for the first cycle. In the last cycle, only 23.7 % and 34.8 % of Cr(VI) was removed with S-TiO_2 and UiO-66-NH_2 as catalyst, respectively. All above-stated experiment illustrated that U1T3 could be reusable. After photocatalytic reactions, the PXRD patterns of used U1T3 corresponded well to those of the original one (Fig. 12d). In addition, the SEM and TEM results (Fig. S16) demonstrated no noticeable changes of the morphology of U1T3 were observed, indicating that U1T3

Table 1
Comparison of photocatalytic properties of various photocatalysts.

Catalyst/dosage (mg L^{-1})	Pollutants/mg L^{-1}	Irradiation	Hole scavenger	Efficiency (%)	k (min^{-1})	Ref
TiO_2@NH_2-MIL-88B(Fe)/500	Cr(VI)/10.4	500 W Xe lamp	$(NH_4)_2C_2O_4$	98.6%	35 min 0.0878	(Yuan et al., 2019)
MIL-100(Fe)/TiO_2/50	$K_2Cr_2O_7$/10	450 W Xe arc lamp	methanol	50.0%	60 min 0.0339	(He et al., 2019)
WO_3/TiO_2	Cr(VI)/20	Xe lamp	citric acid	100.0%	130 min -	(Yang et al., 2010)
SnS_2/TiO_2/1000	$K_2Cr_2O_7$/50	Visible light	/	100.0%	120 min	(Zhang et al., 2012)
Ag/TiO_2 /200	Cr(VI)/10	300 W xenon lamp	/	99.8%	240 min -	(Lei et al., 2014)
S-TiO_2/UiO-66-NH_2/200	Cr(VI)/5	LED visible light (50 mW)	/	100.0%	75 min 0.0704	This work
TiO_2@MIL-101(Cr)/500	BPA/50	125 W mercury lamp	/	92.0%	240 min 0.0024	(Tang et al., 2019)
N-doped TiO_2/500	BPA/5	LED visible light (15 W)	/	90.0%	120 min 0.0224	(Subagio et al., 2010)
S-TiO_2/UiO-66-NH_2/200	BPA/5	LED visible light (50 mW)	/	97.4%	120 min 0.0298	This work

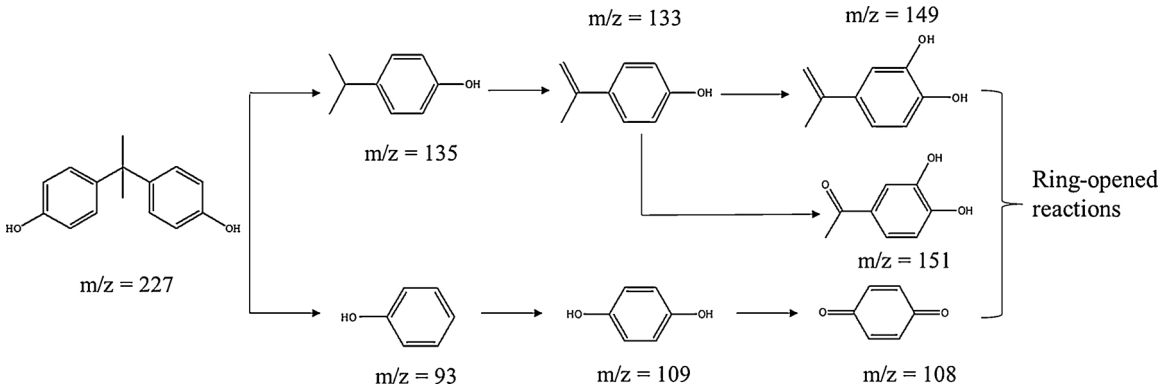

Fig. 11. Possible photocatalytic degradation pathways of BPA degradation.

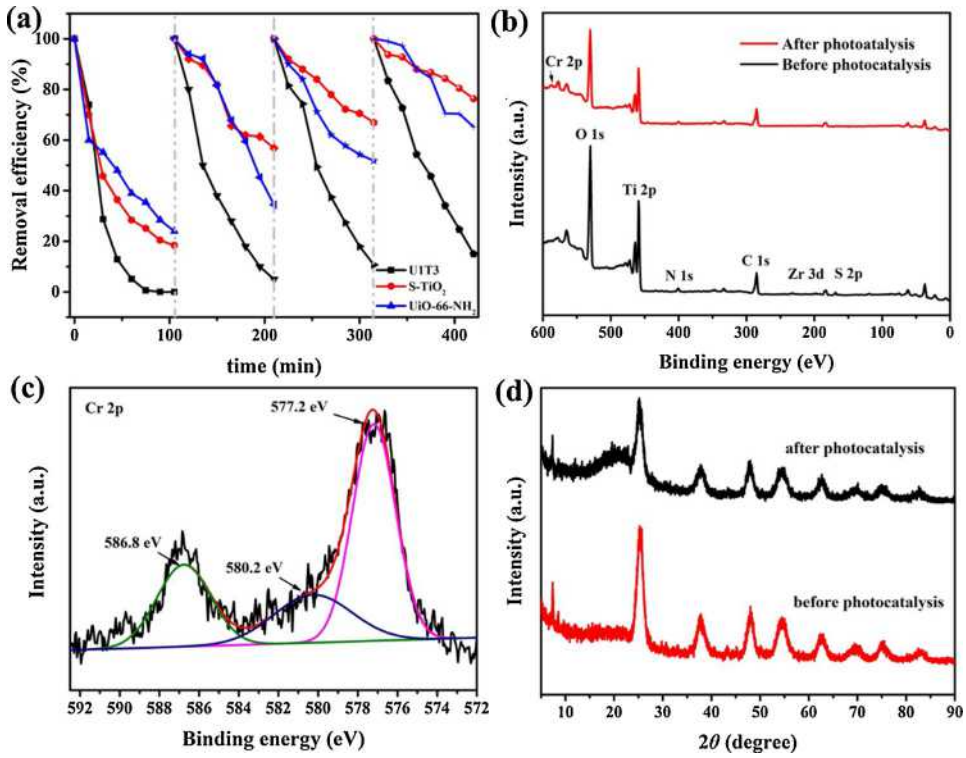

Fig. 12. The cyclic performance of Cr(VI) removal over U1T3, S-TiO_2 and UiO-66-NH_2 (a). XPS survey spectra of U1T3 (b) and Cr 2p spectrum of U1T3 after the photocatalytic activities (c). PXRD patterns of U1T3 (d).

demonstrated good stability. It was worth noting that little amount of titanium and zirconium (< 10 μg L^{-1}) were detected by inductively coupled plasma-optical emission spectrometry (ICP-5000, Focused Photonics Inc.) after four cycles. Overall, the reusable and stable U1T3 is environmentally friendly and efficient as photocatalyst.

3.2.4. Photocatalytic mechanism

The electrochemical impedance spectroscopy (EIS) measurements were conducted to elucidate the photo-generated carrier separation performance of the photocatalyst. It was generally believed that the smaller the arc radius in the Nyquist diagram represented the lower charge transfer resistance (R_{ct}) (Yi et al., 2019a; Yuan et al., 2019). As depicted in Fig. 13a, the diameter of arc radius followed the order of S-TiO_2 > UiO-66-NH_2 > U1T3, demonstrating that U1T3 possessed better charge separation or migration ability than the pristine S-TiO_2 and UiO-66-NH_2. Additionally, the photocurrent spectroscopy was also introduced to evaluate the photocatalytic performances. The photocurrent densities followed the order of U1T3 > S-TiO_2 > UiO-66-NH_2 (Fig. S17). Therefore, U1T3 exhibited higher photogenerated electron-hole separation ability (Chen et al., 2018).

The trapping experiments were used to confirm the photo-produced active species and explore the possible mechanism. The different active species capture agents like $K_2S_2O_8$ (Sharma and Dutta, 2015), benzoquinone (BQ) (Ju et al., 2017), isopropyl alcohol (IPA) (Hwang et al., 2010) and EDTA-2Na (Liu et al., 2013) with identical concentration of 0.2 mmol L^{-1} were recommended to capture e-, ·O_2-, ·OH and h^+, respectively. As demonstrated in Fig. 13b, the Cr(VI) removal efficiencies declined to 97.5 % within 90 min after the addition of $K_2S_2O_8$. When IPA was added into the solution, photocatalytic removal rate decreased, which was attributed to the following chemical equation (Eq.s (8),(9) and (10)) (Yi et al., 2019a). In the presence of EDTA-2Na, photocatalytic Cr(VI) reduction efficiency was promoted obviously, indicating that the consumed holes facilitated the separation of electrons and holes. It was reported that ·O_2- can also take part in the reduction of Cr(VI) (Li et al., 2019a; Zhang et al., 2018b; Wang et al., 2016c). Under the N_2 atmosphere, a slight decrease of Cr(VI) reduction rate was observed, implying that ·O_2- took part in Cr(VI) reduction but exerted minor effect. The main active species of photocatalytic BPA degradation were also investigated. As shown in Fig. 13c, the BPA degradation efficiencies decreased conspicuously with the addition of EDTA-2Na and BQ. Therefore, it can be noted that h^+ and ·O_2- were the predominated active species for photocatalytic BPA oxidation.

$$O_2 + e^- \rightarrow \cdot O_2^- \quad (8)$$

$$2\cdot O_2 + 2H^+ \rightarrow H_2O_2 + O_2 \quad (9)$$

$$H_2O_2 + Cr(III) + H^+ \rightarrow Cr(VI) + H_2O + \cdot OH \quad (10)$$

Based on the obtained results, the II-scheme mechanism of photocatalytic system illustrated in Fig. 14 was proposed over S-TiO_2/UiO-66-NH_2 composites. Both S-TiO_2 and UiO-66-NH_2 could produce electrons and holes when they were exposed to the visible light. The photogenerated electrons were transferred from LOMO of UiO-66-NH_2 to CB of S-TiO_2, due to the potential difference between UiO-66-NH_2's LOMO at -0.6 eV and S-TiO_2's CB at -0.35 eV. ·O_2^- could be produced over both LUMO/CB of UiO-66-NH_2 and S-TiO_2, due to that their potentials were higher than that of O_2/·O_2^- (-0.33 eV *vs*. NHE) (Deng et al., 2017). The ESR measurement also verified the existence of ·O_2^-. As shown in Fig. 13d, the DMPO-·O_2^- signals of U1T3 were detected under visible light for 5 min and 10 min, and no signals were observed in dark, confirming that ·O_2- radicals were generated in the process of photocatalysis.

4. Conclusions

In summary, series S-TiO_2/UiO-66-NH_2 composites were constructed by facile ball-milling method, which exhibited superior photocatalytic efficiencies of Cr(VI) reduction and BPA oxidation than pristine UiO-66-NH_2 and S-TiO_2 under LED visible light. S-TiO_2 was uniformly coated on the surface of UiO-66-NH_2, making a strong chemical interface and enhanced separation of electron-hole pairs between

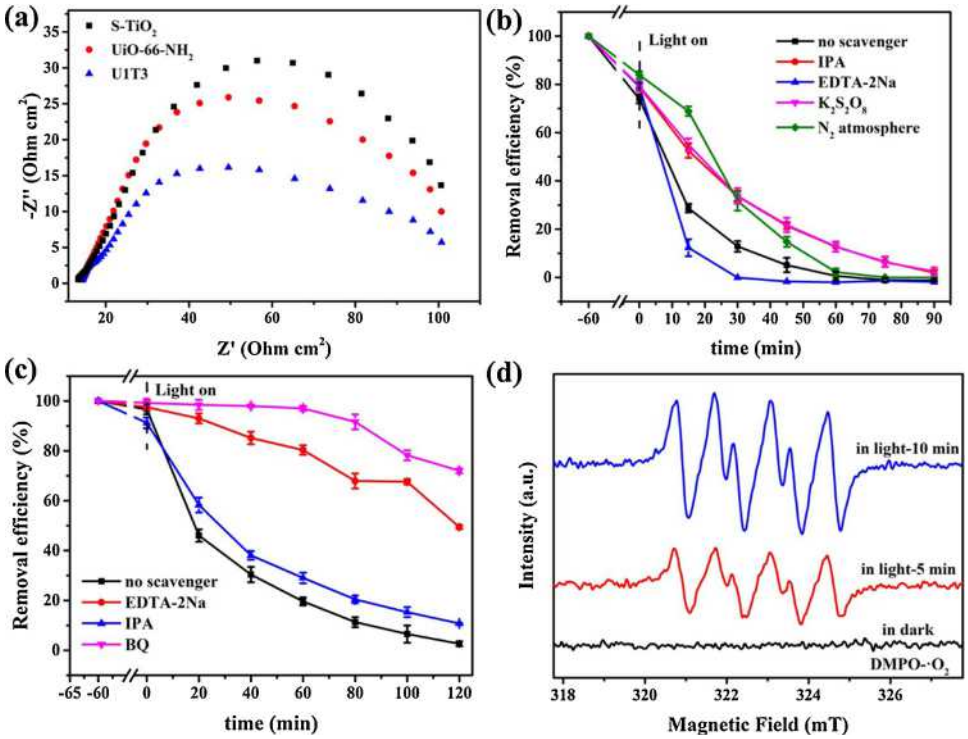

Fig. 13. The Electrochemical impedance spectra over U1T3, S-TiO_2 and UiO-66-NH_2 (a). Effects on Cr(VI) reduction (b) and BPA degradation (c) over U1T3 with different scavengers. the ESR spectra of $\cdot O_2^-$ trapped by DMPO of U1T3 (d).

the two components. The influence factors like pH values and co-existing foreign matters on the photocatalytic removal efficiencies were explored. Therein, the influence of inorganic ions and DOM on Cr(VI) reduction processes was also confirmed by the Box-Behnken design methodology. The possible pathway of photocatalytic BPA degradation was proposed and confirmed by LC–MS analysis. It is worth noting that U1T3 showed good photocatalytic performances under real sunlight. The proposed photocatalysis mechanism was verified by active material capture experiments and Mott-Schottky curves, and further confirmed by ESR determination. Furthermore, the cycling experiments indicated that S-TiO_2/UiO-66-NH_2 composite (U1T3) possessed good reusability and stability. This work provides a promising strategy for construction of doped TiO_2 and MOFs composites to achieve good photocatalytic oxidation and reduction efficiencies in water treatment.

CRediT authorship contribution statement

Yu-Xuan Li: Data curation, Investigation, Visualization, Writing - original draft. **Xun Wang:** Resources, Investigation. **Chong-Chen Wang:** Conceptualization, Funding acquisition, Supervision, Project administration, Writing - review & editing. **Huifen Fu:** Resources, Validation. **Yanbiao Liu:** Resources. **Peng Wang:** Resources. **Chen Zhao:** Resources.

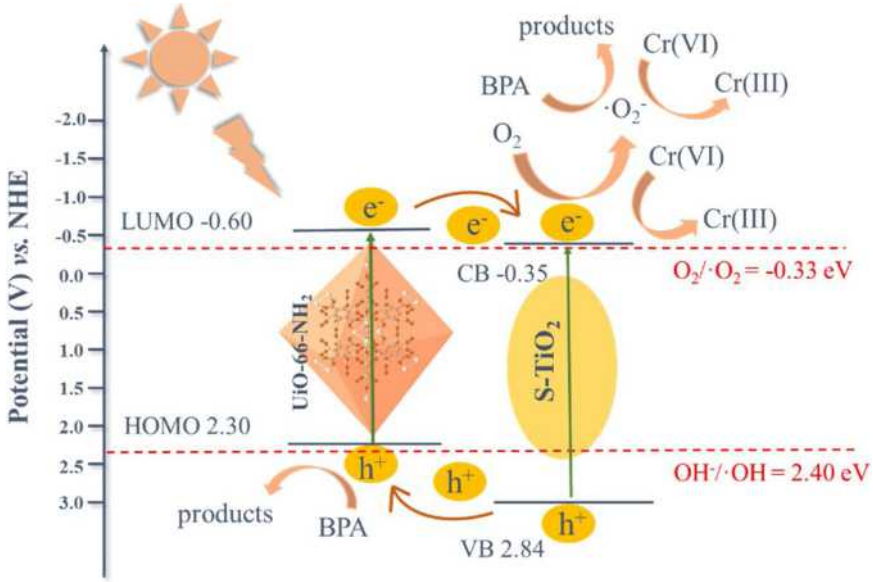

Fig. 14. A possible mechanism for photocatalytic reduction of Cr(VI) and degradation of BPA over U1T3.

Declaration of Competing Interest

The authors declare that they have no known competing financial interests or personal relationships that could have appeared to influence the work reported in this paper.

Acknowledgements

This work was supported by National Natural Science Foundation of China (51878023), Beijing Natural Science Foundation (8202016), Great Wall Scholars Training Program Project of Beijing Municipality Universities (CIT&TCD20180323), and Beijing Talent Project (2019A22).

Appendix A. Supplementary data

Supplementary material related to this article can be found, in the online version, at doi:https://doi.org/10.1016/j.jhazmat.2020.123085.

References

Aguila, B., Sun, Q., Wang, X., O'Rourke, E., Al-Enizi, A.M., Nafady, A., Ma, S., 2018. Lower activation energy for catalytic reactions through Host–Guest cooperation within metal–organic frameworks. Angew. Chem. Int. Ed. 57, 10107–10111.
Arconada, N., Durán, A., Suárez, S., Portela, R., Coronado, J.M., Sánchez, B., Castro, Y., 2009. Synthesis and photocatalytic properties of dense and porous TiO_2-anatase thin films prepared by sol–gel. Appl. Catal., B 86, 1–7.
Bai, S., Yang, L., Wang, C., Lin, Y., Lu, J., Jiang, J., Xiong, Y., 2015. Boosting photocatalytic water splitting: interfacial charge polarization in atomically controlled core–shell cocatalysts. Angew. Chem. Int. Ed. 54, 14810–14814.
Bai, Y., Ye, L., Chen, T., Wang, P., Wang, L., Shi, X., Wong, P.K., 2017. Synthesis of hierarchical bismuth-rich $Bi_4O_5Br_xI_{2-x}$ solid solutions for enhanced photocatalytic activities of CO_2 conversion and Cr(VI) reduction under visible light. Appl. Catal., B 203, 633–640.
Barceló, D., Petrovic, M., 2007. Pharmaceuticals and personal care products (PPCPs). The Environment. Springer.
Canale, F., Cordero, C., Baggiani, C., Baravalle, P., Giovannoli, C., Bicchi, C., 2010. Development of a molecularly imprinted polymer for selective extraction of bisphenol A in water samples. J. Sep. Sci. 33, 1644–1651.
Cariot, A., Dupuis, A., Albouy-Llaty, M., Legube, B., Rabouan, S., Migeot, V., 2012. Reliable quantification of bisphenol A and its chlorinated derivatives in human breast milk using UPLC–MS/MS method. Talanta 100, 175–182.
Chen, X., Yu, T., Fan, X., Zhang, H., Li, Z., Ye, J., Zou, Z., 2007. Enhanced activity of mesoporous Nb_2O_5 for photocatalytic hydrogen production. Appl. Surf. Sci. 253, 8500–8506.
Chen, D., Xing, H., Wang, C., Su, Z., 2016. Highly efficient visible-light-driven CO_2 reduction to formate by a new anthracene-based zirconium MOF via dual catalytic routes. J. Mater. Chem. A 4, 2657–2662.
Chen, F., Yang, Q., Wang, Y., Yao, F., Ma, Y., Huang, X., Li, X., Wang, D., Zeng, G., Yu, H., 2018. Efficient construction of bismuth vanadate-based Z-scheme photocatalyst for simultaneous Cr(VI) reduction and ciprofloxacin oxidation under visible light: kinetics, degradation pathways and mechanism. Chem. Eng. J. 348, 157–170.
Chen, D.-D., Yi, X.-H., Zhao, C., Fu, H., Wang, P., Wang, C.-C., 2020. Polyaniline modified MIL-100(Fe) for enhanced photocatalytic Cr(VI) reduction and tetracycline degradation under white light. Chemosphere 245, 125659.
Chiang, K., Lim, T.M., Tsen, L., Lee, C.C., 2004. Photocatalytic degradation and mineralization of bisphenol A by TiO_2 and platinized TiO_2. Appl. Catal., A 261, 225–237.
Coronado, J.M., Kataoka, S., Tejedor-Tejedor, I., Anderson, M.A., 2003. Dynamic phenomena during the photocatalytic oxidation of ethanol and acetone over nanocrystalline TiO_2: simultaneous FTIR analysis of gas and surface species. J. Catal. 219, 219–230.
Deng, Y., Tang, L., Zeng, G., Feng, C., Dong, H., Wang, J., Feng, H., Liu, Y., Zhou, Y., Pang, Y., 2017. Plasmonic resonance excited dual Z-scheme $BiVO_4/Ag/Cu_2O$ nanocomposite: synthesis and mechanism for enhanced photocatalytic performance in recalcitrant antibiotic degradation. Environ. Sci. Nano 4, 1494–1511.
Du, X., Yi, X., Wang, P., Deng, J., Wang, C.-C., 2019a. Enhanced photocatalytic Cr(VI) reduction and diclofenac sodium degradation under simulated sunlight irradiation over MIL-100(Fe)/g-C_3N_4 heterojunctions. Chin. J. Catal. 40, 70–79.
Du, X.-D., Yi, X.-H., Wang, P., Zheng, W., Deng, J., Wang, C.-C., 2019b. Robust photocatalytic reduction of Cr(VI) on UiO-66-NH_2(Zr/Hf) metal-organic framework membrane under sunlight irradiation. Chem. Eng. J. 356, 393–399.
Ellis, J.B., 2006. Pharmaceutical and personal care products (PPCPs) in urban receiving waters. Environ. Pollut. 144, 184–189.
Gao, P., Liu, J., Zhang, T., Sun, D.D., Ng, W., 2012. Hierarchical TiO_2/CdS "spindle-like" composite with high photodegradation and antibacterial capability under visible light irradiation. J. Hazard. Mater. 229–230, 209–216.
Grover, I.S., Singh, S., Pal, B., 2013. The preparation, surface structure, zeta potential, surface charge density and photocatalytic activity of TiO_2 nanostructures of different shapes. Appl. Surf. Sci. 280, 366–372.
Guo, J., Li, J.-J., Wang, C.-C., 2019. Adsorptive removal of Cr(VI) from simulated wastewater in MOF BUC-17 ultrafine powder. J. Environ. Chem. Eng. 7, 102909.
He, X., Fang, H., Gosztola, D.J., Jiang, Z., Jena, P., Wang, W.-N., 2019. Mechanistic insight into photocatalytic pathways of MIL-100(Fe)/TiO_2 composites. ACS Applied Materials & Interfaces 11, 12516–12524.
Ho, W., Yu, J.C., Lee, S., 2006. Low-temperature hydrothermal synthesis of S-doped TiO_2 with visible light photocatalytic activity. J. Solid State Chem. 179, 1171–1176.
Hu, J., Chen, G., Lo, I.M.C., 2005. Removal and recovery of Cr(VI) from wastewater by maghemite nanoparticles. Water Res. 39, 4528–4536.
Huo, R., Yang, J.-Y., Liu, Y.-Q., Liu, H.-F., Li, X., Xu, Y.-H., 2016. Preparation of W and N, S-codoped titanium dioxide with enhanced photocatalytic activity under visible light irradiation. Mater. Res. Bull. 76, 72–78.
Hwang, S., Huling, S.G., Ko, S., 2010. Fenton-like degradation of MTBE: effects of iron counter anion and radical scavengers. Chemosphere 78, 563–568.
Irie, H., Kamiya, K., Shibanuma, T., Miura, S., Tryk, D.A., Yokoyama, T., Hashimoto, K., 2009. Visible light-sensitive Cu(II)-grafted TiO_2 photocatalysts: activities and X-ray absorption fine structure analyses. J. Phy. Chem. C 113, 10761–10766.
Iwasaki, M., Hara, M., Kawada, H., Tada, H., Ito, S., 2000. Cobalt ion-doped TiO_2 photocatalyst response to visible light. J. Colloid Interface Sci. 224, 202–204.
Ju, L., Wu, P., Lai, X., Yang, S., Gong, B., Chen, M., Zhu, N., 2017. Synthesis and characterization of fullerene modified ZnAlTi-LDO in photo-degradation of bisphenol A under simulated visible light irradiation. Environ. Pollut. 228, 234–244.
Karthik, P., Vinoth, R., Zhang, P., Choi, W., Balaraman, E., Neppolian, B., 2018. π–π interaction between metal–organic framework and reduced graphene oxide for visible-light photocatalytic H_2 production. ACS Applied Energy Materials 1, 1913–1923.
Kim, S., Hwang, S.-J., Choi, W., 2005. Visible light active platinum-ion-doped TiO_2 photocatalyst. The Journal of Physical Chemistry B 109, 24260–24267.
Lee, S.-Y., Park, S.-J., 2013. TiO_2 photocatalyst for water treatment applications. J. Ind. Eng. Chem. 19, 1761–1769.
Lei, X.F., Xue, X.X., Yang, H., 2014. Preparation and characterization of Ag-doped TiO_2 nanomaterials and their photocatalytic reduction of Cr(VI) under visible light. Appl. Surf. Sci. 321, 396–403.
Li, X.Z., Li, F.B., Yang, C.L., Ge, W.K., 2001. Photocatalytic activity of WO_x-TiO_2 under visible light irradiation. J. Photochem. Photobiol., A 141, 209–217.
Li, D., Haneda, H., Hishita, S., Ohashi, N., 2005. Visible-light-driven n−f−codoped TiO_2 photocatalysts. 1. synthesis by spray pyrolysis and surface characterization. Chem. Mater. 17, 2588–2595.
Li, L., Xu, Z., Liu, F., Shao, Y., Wang, J., Wan, H., Zheng, S., 2010. Photocatalytic nitrate reduction over Pt–Cu/TiO_2 catalysts with benzene as hole scavenger. J. Photochem. Photobiol., A 212, 113–121.
Li, Y.-X., Fu, H., Wang, P., Zhao, C., Liu, W., Wang, C.-C., 2019a. Porous tube-like ZnS derived from rod-like ZIF-L for photocatalytic Cr(VI) reduction and organic pollutants degradation. Environ. Pollut., 113417.
Li, P., Guo, M., Wang, Q., Li, Z., Wang, C., Chen, N., Wang, C.-C., Wan, C., Chen, S., 2019b. Controllable synthesis of cerium zirconium oxide nanocomposites and their application for photocatalytic degradation of sulfonamides. Appl. Catal., B 259, 118107.
Li, M., Liu, F., Ma, Z., Liu, W., Liang, J., Tong, M., 2019c. Different mechanisms for E. Coli disinfection and BPA degradation by CeO_2-AgI under visible light irradiation. Chem. Eng. J. 371, 750–758.
Liu, Y., Deng, L., Chen, Y., Wu, F., Deng, N., 2007. Simultaneous photocatalytic reduction of Cr(VI) and oxidation of bisphenol A induced by Fe(III)–OH complexes in water. J. Hazard. Mater. 139, 399–402.
Liu, J., Wang, Z., Liu, L., Chen, W., 2011. Reduced graphene oxide as capturer of dyes and electrons during photocatalysis: surface wrapping and capture promoted efficiency. PCCP 13, 13216–13221.
Liu, Y., Zhu, Y., Xu, J., Bai, X., Zong, R., Zhu, Y., 2013. Degradation and mineralization mechanism of phenol by $BiPO_4$ photocatalysis assisted with H_2O_2. Appl. Catal., B 142–143, 561–567.
Liu, J., Cheng, B., Yu, J., 2016. A new understanding of the photocatalytic mechanism of the direct Z-scheme g-C_3N_4/TiO_2 heterostructure. PCCP 18, 31175–31183.
Lu, N., Lu, Y., Liu, F., Zhao, K., Yuan, X., Zhao, Y., Li, Y., Qin, H., Zhu, J., 2013. $H_3PW_{12}O_{40}$/TiO_2 catalyst-induced photodegradation of bisphenol A (BPA): kinetics, toxicity and degradation pathways. Chemosphere 91, 1266–1272.
Luo, J., Zhang, S., Sun, M., Yang, L., Luo, S., Crittenden, J.C., 2019. A critical review on energy conversion and environmental remediation of photocatalysts with remodeling crystal lattice, surface, and interface. ACS Nano 13, 9811–9840.
Ma, D., Xin, Y., Gao, M., Wu, J., 2014. Fabrication and photocatalytic properties of cationic and anionic S-doped TiO_2 nanofibers by electrospinning. Appl. Catal., B 147, 49–57.
Machado, T.C., Lansarin, M.A., Matte, N., 2014. Reduction of hexavalent chromium: photocatalysis and photochemistry and their application in wastewater remediation. Water Sci. Technol. 70, 55–61.
Molkenthin, M., Olmez-Hanci, T., Jekel, M.R., Arslan-Alaton, I., 2013. Photo-fenton-like treatment of BPA: effect of UV light source and water matrix on toxicity and transformation products. Water Res. 47, 5052–5064.
Ohko, Y., Ando, I., Niwa, C., Tatsuma, T., Yamamura, T., Nakashima, T., Kubota, Y., Fujishima, A., 2001. Degradation of bisphenol a in Water by TiO_2 photocatalyst. Environmental Science & Technology 35, 2365–2368.
Ohno, T., Akiyoshi, M., Umebayashi, T., Asai, K., Mitsui, T., Matsumura, M., 2004. Preparation of S-doped TiO_2 photocatalysts and their photocatalytic activities under visible light. Appl. Catal., A 265, 115–121.
Rammelt, U., Hebestreit, N., Fikus, A., Plieth, W., 2001. Investigation of polybithiophene/n-TiO_2 bilayers by electrochemical impedance spectroscopy and photoelectrochemistry. Electrochim. Acta 46, 2363–2371.

Seh, Z.W., Liu, S., Low, M., Zhang, S.-Y., Liu, Z., Mlayah, A., Han, M.-Y., 2012. Janus Au-TiO_2 photocatalysts with strong localization of plasmonic near-fields for efficient visible-light hydrogen generation. Adv. Mater. 24, 2310–2314.
Sharma, A., Dutta, R.K., 2015. Studies on the drastic improvement of photocatalytic degradation of acid orange-74 dye by TPPO capped CuO nanoparticles in tandem with suitable electron capturing agents. RSC Adv. 5, 43815–43823.
Sharma, J., Mishra, I.M., Dionysiou, D.D., Kumar, V., 2015. Oxidative removal of bisphenol a by UV-C/peroxymonosulfate (PMS): kinetics, influence of co-existing chemicals and degradation pathway. Chem. Eng. J. 276, 193–204.
Shi, L.-n., Zhang, X., Chen, Z.-l., 2011. Removal of chromium (VI) from wastewater using bentonite-supported nanoscale zero-valent iron. Water Res. 45, 886–892.
Song, T., Zhang, L., Zhang, P., Zeng, J., Wang, T., Ali, A., Zeng, H., 2017. Stable and improved visible-light photocatalytic hydrogen evolution using copper(ii)–organic frameworks: engineering the crystal structures. J. Mater. Chem. A 5, 6013–6018.
Su, Y., Liu, S.Y., Tang, W.H., 2012. Photodecomposition of methylene Blue by the S, Al doped TiO_2 mesoporous materials. Adv. Mater. Res. 499, 58–62.
Subagio, D.P., Srinivasan, M., Lim, M., Lim, T.-T., 2010. Photocatalytic degradation of bisphenol A by nitrogen-doped TiO_2 hollow sphere in a vis-LED photoreactor. Appl. Catal., B 95, 414–422.
Subramanian, V., Karki, A., Gnanasekar, K.I., Eddy, F.P., Rambabu, B., 2006. Nanocrystalline TiO_2 (anatase) for Li-ion batteries. J. Power Sources 159, 186–192.
Tang, Y., Yin, X., Mu, M., Jiang, Y., Li, X., Zhang, H., Ouyang, T., 2019. A novel anatase TiO_2@ MIL-101 (Cr) nanocomposite for photocatalytic degradation of bisphenol A. Beilstein Archives 2019, 141.
Testa, J.J., Grela, M.A., Litter, M.I., 2004. Heterogeneous photocatalytic reduction of chromium(VI) over TiO_2 particles in the presence of oxalate: involvement of Cr(V) species. Environmental Science & Technology 38, 1589–1594.
Tsai, W.-T., Lee, M.-K., Su, T.-Y., Chang, Y.-M., 2009. Photodegradation of bisphenol A in a batch TiO_2 suspension reactor. J. Hazard. Mater. 168, 269–275.
Velegraki, G., Miao, J., Drivas, C., Liu, B., Kennou, S., Armatas, G.S., 2018. Fabrication of 3D mesoporous networks of assembled CoO nanoparticles for efficient photocatalytic reduction of aqueous Cr(VI). Appl. Catal., B 221, 635–644.
Wang, K.-H., Hsieh, Y.-H., Wu, C.-H., Chang, C.-Y., 2000. The pH and anion effects on the heterogeneous photocatalytic degradation of o-methylbenzoic acid in TiO_2 aqueous suspension. Chemosphere 40, 389–394.
Wang, Y., Li, J., Peng, P., Lu, T., Wang, L., 2008. Preparation of S-TiO_2 photocatalyst and photodegradation of L-acid under visible light. Appl. Surf. Sci. 254, 5276–5280.
Wang, Y., Sun, Y., Li, K., 2009. Dye-sensitized solar cells based on oriented ZnO nanowire-covered TiO_2 nanoparticle composite film electrodes. Mater. Lett. 63, 1102–1104.
Wang, P., Yap, P.-S., Lim, T.-T., 2011. C–N–S tridoped TiO_2 for photocatalytic degradation of tetracycline under visible-light irradiation. Appl. Catal., A 399, 252–261.
Wang, C., Zhu, L., Wei, M., Chen, P., Shan, G., 2012. Photolytic reaction mechanism and impacts of coexisting substances on photodegradation of bisphenol A by Bi_2WO_6 in water. Water Res. 46, 845–853.
Wang, C.-C., Li, J.-R., Lv, X.-L., Zhang, Y.-Q., Guo, G., 2014. Photocatalytic organic pollutants degradation in metal–organic frameworks. Energy & Environmental Science 7, 2831–2867.
Wang, C.-C., Du, X.-D., Li, J., Guo, X.-X., Wang, P., Zhang, J., 2016a. Photocatalytic Cr(VI) reduction in metal-organic frameworks: a mini-review. Appl. Catal., B 193, 198–216.
Wang, C.-Y., Zhang, X., Song, X.-N., Wang, W.-K., Yu, H.-Q., 2016b. Novel $Bi_{12}O_{15}Cl_6$ photocatalyst for the degradation of bisphenol A under visible-light irradiation. ACS Applied Materials & Interfaces 8, 5320–5326.
Wang, J.-C., Ren, J., Yao, H.-C., Zhang, L., Wang, J.-S., Zang, S.-Q., Han, L.-F., Li, Z.-J., 2016c. Synergistic photocatalysis of Cr(VI) reduction and 4-chlorophenol degradation over hydroxylated α-Fe_2O_3 under visible light irradiation. J. Hazard. Mater. 311, 11–19.
Wang, Y., Kang, C., Huang, D., Xiao, K., Zhu, L., Liu, F., Tian, T., 2018. Hydrothermal in situ synthesis of Rb and S co-doped Ti-based TiO_2 sheet with a thin film showing high photocatalytic activities. RSC Adv. 8, 11247–11254.
Wang, X., Liu, W., Fu, H., Yi, X.-H., Wang, P., Zhao, C., Wang, C.-C., Zheng, W., 2019a. Simultaneous Cr(VI) reduction and Cr(III) removal of bifunctional MOF/Titanate nanotube composites. Environ. Pollut. 249, 502–511.
Wang, C.-C., Wang, X., Liu, W., 2020b. The synthesis strategies and photocatalytic performances of TiO_2/MOFs composites: a state-of-the-art review. Chem. Eng. J. 391, 123601.
Xing, M., Zhang, J., Chen, F., 2009. New approaches to prepare nitrogen-doped TiO_2 photocatalysts and study on their photocatalytic activities in visible light. Appl. Catal., B 89, 563–569.
Xu, J., Wu, L., Chang, A.C., 2009. Degradation and adsorption of selected pharmaceuticals and personal care products (PPCPs) in agricultural soils. Chemosphere 77, 1299–1305.
Xu, X.-Y., Chu, C., Fu, H., Du, X.-D., Wang, P., Zheng, W., Wang, C.-C., 2018. Light-responsive UiO-66-NH_2/Ag_3PO_4 MOF-nanoparticle composites for the capture and release of sulfamethoxazole. Chem. Eng. J. 350, 436–444.
Yang, L., Xiao, Y., Liu, S., Li, Y., Cai, Q., Luo, S., Zeng, G., 2010. Photocatalytic reduction of Cr(VI) on WO_3 doped long TiO_2 nanotube arrays in the presence of citric acid. Appl. Catal., B 94, 142–149.
Yang, J., Dai, Y., Zhu, X., Wang, Z., Li, Y., Zhuang, Q., Shi, J., Gu, J., 2015. Metal–organic frameworks with inherent recognition sites for selective phosphate sensing through their coordination-induced fluorescence enhancement effect. J. Mater. Chem. A 3, 7445–7452.
Yi, X.-H., Ma, S.-Q., Du, X.-D., Zhao, C., Fu, H., Wang, P., Wang, C.-C., 2019a. The facile fabrication of 2D/3D Z-scheme g-C_3N_4/UiO-66 heterojunction with enhanced photocatalytic Cr(VI) reduction performance under white light. Chem. Eng. J. 375, 121944.
Yi, X.-H., Wang, F.-X., Du, X.-D., Wang, P., Wang, C.-C., 2019b. Facile fabrication of BUC-21/g-C_3N_4 composites and their enhanced photocatalytic Cr(VI) reduction performances under simulated sunlight. Appl. Organomet. Chem. 33, e4621.
Yin, R., Ling, L., Xiang, Y., Yang, Y., Bokare, A.D., Shang, C., 2018. Enhanced photocatalytic reduction of chromium (VI) by Cu-doped TiO_2 under UV-a irradiation. Sep. Purif. Technol. 190, 53–59.
Yoon, J., Shim, E., Bae, S., Joo, H., 2009. Application of immobilized nanotubular TiO_2 electrode for photocatalytic hydrogen evolution: reduction of hexavalent chromium (Cr(VI)) in water. J. Hazard. Mater. 161, 1069–1074.
Yuan, R., Yue, C., Qiu, J., Liu, F., Li, A., 2019. Highly efficient sunlight-driven reduction of Cr(VI) by TiO_2@NH_2-MIL-88B(Fe) heterostructures under neutral conditions. Appl. Catal., B 251, 229–239.
Zhang, Y., Park, S.-J., 2019. Stabilization of dispersed CuPd bimetallic alloy nanoparticles on ZIF-8 for photoreduction of Cr(VI) in aqueous solution. Chem. Eng. J. 369, 353–362.
Zhang, J., Wang, C.-C., 2017. Three two-dimensional coordination polymers constructed from transition metals and 2,3-norbornanedicarboxylic acid: hydrothermal synthesis, crystal structures and photocatalytic properties. J. Mol. Struct. 1130, 223–230.
Zhang, X., Zhang, L., Xie, T., Wang, D., 2009. Low-temperature synthesis and High visible-light-induced photocatalytic activity of BiOI/TiO_2 heterostructures. J. Phys. Chem. C 113, 7371–7378.
Zhang, Y.C., Li, J., Xu, H.Y., 2012. One-step in situ solvothermal synthesis of SnS_2/TiO_2 nanocomposites with high performance in visible light-driven photocatalytic reduction of aqueous Cr(VI). Appl. Catal., B 123–124, 18–26.
Zhang, Y., Zhang, D., Zhou, L., Zhao, Y., Chen, J., Chen, Z., Wang, F., 2018a. Polypyrrole/reduced graphene oxide aerogel particle electrodes for high-efficiency electro-catalytic synergistic removal of Cr(VI) and bisphenol A. Chem. Eng. J. 336, 690–700.
Zhang, F., Zhang, Y., Zhang, G., Yang, Z., Dionysiou, D.D., Zhu, A., 2018b. Exceptional synergistic enhancement of the photocatalytic activity of SnS_2 by coupling with polyaniline and N-doped reduced graphene oxide. Appl. Catal., B 236, 53–63.
Zhao, J., Han, Q., Zhu, J., Wu, X., Wang, X., 2014. Synthesis of Bi nanowire networks and their superior photocatalytic activity for Cr(VI) reduction. Nanoscale 6, 10062–10070.
Zhao, Y., Huang, X., Tan, X., Yu, T., Li, X., Yang, L., Wang, S., 2016. Fabrication of BiOBr nanosheets@TiO_2 nanobelts p–n junction photocatalysts for enhanced visible-light activity. Appl. Surf. Sci. 365, 209–217.
Zhao, C., Wang, Z., Li, X., Yi, X., Chu, H., Chen, X., Wang, C.-C., 2020. Facile fabrication of BUC-21/$Bi_{24}O_{31}Br_{10}$ composites for enhanced photocatalytic Cr(VI) reduction under white light. Chem. Eng. J. 389, 123431.
Zhou, Y.-C., Xu, X.-Y., Wang, P., Fu, H., Zhao, C., Wang, C.-C., 2019. Facile fabrication and enhanced photocatalytic performance of visible light responsive UiO-66-NH_2/Ag_2CO_3 composite. Chin. J. Catal. 40, 1912–1923.
Zou, J.-P., Wu, D.-D., Luo, J., Xing, Q.-J., Luo, X.-B., Dong, W.-H., Luo, S.-L., Du, H.-M., Suib, S.L., 2016. A strategy for one-pot conversion of organic pollutants into useful hydrocarbons through coupling photodegradation of MB with photoreduction of CO_2. ACS Catal. 6, 6861–6867.